Journal of Marine Systems 211 (2020) 103419

Contents lists available at ScienceDirect

Journal of Marine Systems

journal homepage: www.elsevier.com/locate/jmarsys

Amazon River propagation evidenced by a CO_2 decrease at 8°N, 38°W in September 2013

Nathalie Lefèvre[a,*], Pedro Tyaquiçã[a], Doris Veleda[b], Coralie Perruche[c], Simon Jan van Gennip[c]

[a] LOCEAN, Sorbonne Université (Université P. et M. Curie-IRD-CNRS-MNHN), Paris, France
[b] Department of Oceanography, DOCEAN, Federal University of Pernambuco (UFPE), Recife, Brazil
[c] Mercator-Ocean, Ramonville, Saint-Agne, Haute Garonne, France

ARTICLE INFO

Keywords:
Fugacity of CO_2
Air-sea flux of CO_2
Western tropical Atlantic
Amazon plume

ABSTRACT

The surface fugacity of CO_2 (fCO_2) has been measured hourly at a mooring at 8°N, 38°W, using a spectrophotometric CO_2 sensor, from June to October 2013. In September 2013, the fCO_2 and the sea surface salinity (SSS) decrease significantly. The high precipitation due to the presence of the Intertropical Convergence Zone (ITCZ) and the propagation of low salinity waters from the Amazon River plume explain the decrease of SSS. Indeed, in fall, the retroflection of the North Brazil Current (NBC) feeds the North Equatorial Counter Current (NECC) and transports Amazon waters to the eastern part of the tropical Atlantic. Simulations from a three dimensional physical and biogeochemical model and observations at the mooring show that the Amazon plume reached the mooring in September 2013. The decrease of fCO_2 is associated with a moderate peak of chlorophyll. Over the period of the CO_2 observations, the site is a source of CO_2 to the atmosphere of 0.65 ± 0.47 mmol m^{-2} day^{-1}. Although the wind speed is at its lowest intensity in September 2013, the flux over the whole period would be about 14% higher without this month. Every month of September from 2006 to 2017, the model simulates a decrease of dissolved inorganic carbon corresponding to the SSS minimum.

1. Introduction

The tropics are regions of large outgassing of CO_2 due to high temperatures and to CO_2-rich waters coming up to the surface. The flux of CO_2 is a function of the difference in the fugacity of CO_2 (fCO_2) between the ocean and the atmosphere. Because the atmospheric fCO_2 is relatively constant, the CO_2 flux is mainly controlled by variations of fCO_2 in seawater. The seawater fCO_2 is linked to pH, alkalinity (TA) and dissolved inorganic carbon (DIC) through the equations of the carbonate system. Alkalinity usually follows the salinity distribution as it is mainly affected by evaporation and precipitation. Alkalinity tends to have higher values at low latitudes than at high latitudes. DIC tends to follow the general pattern of surface temperature and has lower values at low latitudes compared to higher latitudes. In the tropics, TA and DIC are strongly correlated (Williams and Follows, 2011). TA and DIC have opposite effects on seawater fCO_2: an increase of TA would decrease fCO_2 whereas an increase of DIC would increase fCO_2.

Most of the studies on the CO_2 fluxes in the tropics have focused on the Pacific because of the strong interannual variability associated with the El Niño Southern Oscillation (ENSO). The tropical Atlantic, in contrast, has been little studied (Wang et al., 2015) despite showing complex physical dynamics. Within the Western Tropical Atlantic (WTA), opposing mechanisms exist acting as sources or sinks of CO_2 for the atmosphere: on one hand, the equatorial upwelling and the warm temperatures dominating the tropical Atlantic make it a source of CO_2 to the atmosphere; on the other hand, the supply of freshwater from the Amazon River has a significant impact on the stratification and on the salinity distribution of the Atlantic (e.g. Varona et al., 2019).

In addition, the nutrient loads carried by the Amazon and discharged into the oceanic region increase the primary production (DeMaster and Pope, 1996; Smith and Demaster, 1996; Subramaniam et al., 2008) and lead to substantial CO_2 drawdowns (Cooley and Yager, 2006; Körtzinger, 2003, 2010; Lefèvre et al., 2010; Ternon et al., 2000). These studies on the CO_2 drawdowns have evidenced the strong correlation between the surface fugacity of CO_2 (fCO_2) and the sea surface salinity (SSS) with very low fCO_2 associated to the lowest SSS. Both river discharge and rainfall contribute to decrease the SSS. The spreading of the Amazon plume varies seasonally depending on the seasonal migration of the Intertropical Convergence Zone (ITCZ). The ITCZ is located in the zone of confluence of the trade winds. In boreal winter, the ITCZ is at its southernmost position and the North Brazil Current (NBC) is under the influence of the northeast trade winds,

* Corresponding author.
E-mail address: nathalie.lefevre@locean-ipsl.upmc.fr (N. Lefèvre).

https://doi.org/10.1016/j.jmarsys.2020.103419
Received 3 December 2019; Received in revised form 14 July 2020; Accepted 15 July 2020
Available online 20 July 2020

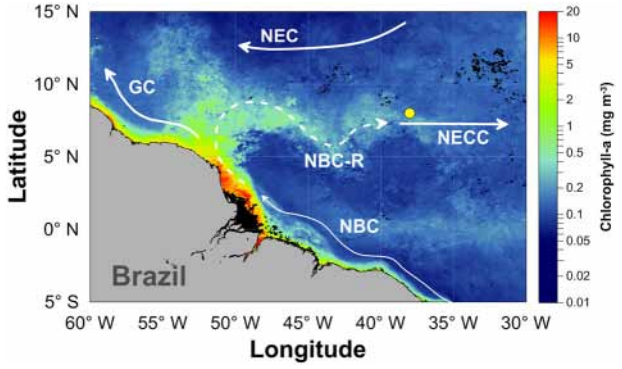

Fig. 1. Main surface currents in the Western Tropical Atlantic. A MODIS Aqua chlorophyll *a* (mg m^{-3}) composite of September 2013 highlights the North Brazil Current (NBC) retroflection.

remaining confined to the coast and flowing northwestward. In boreal summer and autumn, the southeasterly winds prevail and the ITCZ is at its northernmost position. The NBC is under the influence of the southeast trade winds, and then it becomes detached from the coast at about 7-8°N and retroflects eastward (Fig. 1). The NBC retroflection feeds the North Equatorial Countercurrent (NECC) flowing eastward and carrying surface waters, rich in nutrients, from the Amazon River plume (Coles et al., 2013; Fonseca et al., 2004; Hu et al., 2004).

For a complete overview of the current system in the tropical Atlantic, we refer the reader to Fig. 1 of Bruto et al. (2017). At this time of the year, the CO_2 undersaturation observed in the plume may be encountered very far offshore due to the slow air-sea exchange (Ibánhez et al., 2016; Lefèvre et al., 1998). In boreal spring and winter, the northeasterly winds are dominant, the ITCZ is further south, and the Amazon River plume is smaller and more confined near the coast, with a transport mainly northwestward.

In addition to the river discharge, rainfall due to the ITCZ is also a significant freshwater supply. Precipitation decreases fCO_2 and leads to CO_2 undersaturation especially in the ITCZ (Lefèvre et al., 2010; Turk et al., 2010). The propagation of CO_2 undersaturations and their impact on the CO_2 budget of the tropical Atlantic, and on its variability, are still poorly known. A better understanding of the fCO_2 distribution including the processes affecting its variability is needed.

In the Western Tropical Atlantic, the mooring station at 8°N, 38°W, equipped with a CARIOCA (Carbon Interface Ocean Atmosphere) CO_2 sensor to monitor the surface fCO_2, offers great insight into the fCO_2 variability of the region and enables to study the different mechanisms at play. Using data from 2008 to 2011, Bruto et al. (2017) found that fCO_2 was correlated with sea surface temperature variations during January to July whereas from August to December the fCO_2 variability was very complex with several processes occurring simultaneously. Performing a salt budget from the moored buoys along 38°W, Foltz et al. (2004) showed that the precipitation and the zonal advection were particularly important during summer and fall at 8°N. Examining the transport of low-salinity water, Foltz et al. (2015) conclude that the presence of the Amazon plume is not systematically observed at this site. The reason is that the plume reaches its easternmost extension at 38°W. According to their analysis for the period 1998–2013, the plume arrives at the mooring in 2001, 2003, 2009 and 2011. However, using a 1/6° model, Coles et al. (2013) report the Amazon influence beyond the station, as far as 20°W, and conclude that the impact of the Amazon River at 8°N, 38°W is similar to that of precipitation.

In this paper, we focus on the data of 2013 obtained at 8°N, 38°W. Using in situ and satellite data as well as model simulations, we examine the processes affecting the distribution of fCO_2 at this site. In particular, we address whether the propagation of the Amazon plume is observed and how it affects the sea-air CO_2 flux at the mooring.

2. Material and methods

2.1. Measurements at the PIRATA site 8°N, 38°W

An instrumented buoy was deployed at 8°N, 38°W on 18 June 2013 as part of the PIRATA (Prediction Research Moored Array in the Atlantic) program, a network of moored buoys installed in the Atlantic since 1997 (Bourlès et al., 2019). The CARIOCA sensor measured hourly surface fCO_2, at about 1.5 m depth, from 19 June to 13 October 2013 at 8°N, 38°W. The accuracy of the fCO_2 measurements, made by spectrophotometry using thymol blue, is estimated at ± 3 µatm (Hood and Merlivat, 2001). The CARIOCA sensor has been deployed during the PIRATA Brazilian cruise for servicing the moorings of the Western Tropical Atlantic. At 8°N, 38°W the instrumented buoy measures seawater temperature at 1 m, 20 m, 40 m, 60 m, 80 m, 100 m, 120 m, 140 m, 180 m, 300 m, 500 m, salinity at 1 m, 20 m, 40 m, 80 m, 120 m, shortwave radiation, precipitation, relative humidity, air temperature and wind. However, in 2013, the anemometer did not work and the surface salinity sensor stopped working after 23 July 2013. We use the procedure of gap-filling described by Foltz et al. (2015) to reconstruct the SSS from the salinity measured at 20 m. The method consists of using the salinity at a deeper level after correcting it by a seasonal bias. We calculated a climatology of the difference between salinity at 20 m and SSS from 2006 to 2017. The daily climatology of the difference was then subtracted from the daily salinity at 20 m to reconstruct the daily SSS from July to December 2013. This method reproduces the observed SSS as shown by the comparison between observed and reconstructed SSS from 2006 to 2017 (Fig. S1). Gaps remain when no data are available.

During the PIRATA Brazilian cruises in 2009, 2010, 2011, 2014 and 2015, surface seawater samples were taken at 8°N, 38°W for DIC and TA determination. The samples were poisoned with a saturated $HgCl_2$ solution and they were analyzed back in the laboratory LOCEAN, in Paris, using a closed-cell potentiometric titration (Edmond, 1970). Prof. A. Dickson (Scripps Institution of Oceanography, San Diego, USA) provided the Certified Reference Materials (CRMs) that were used for calibration. The accuracy of DIC is estimated at 3 µmol/kg.

2.2. CO_2 flux calculation

The CO_2 flux is calculated using the following expression:

$$F = k\, So\, (fCO_2 - fCO_{2atm}) \quad (1)$$

where So is the solubility of Weiss (1974) and fCO_{2atm} is the atmospheric fugacity of CO_2. k is the gas exchange coefficient of Sweeney et al. (2007) and is given by:

$$k = 0.27\, U_{10}^2\, (Sc/660)^{-0.5} \quad (2)$$

where U_{10} is the wind speed at 10 m above sea level and *Sc* is the Schmidt number.

The wind speed at 10 m is available from the Copernicus Climate Change Service (C3S), ERA5 dataset available at https://cds.climate.copernicus.eu/cdsapp#!/home. The 6-hourly wind speeds from the cross-calibrated multi-platform version 2 (CCMP2 Wentz et al., 2015) are averaged daily and are used to calculate the CO_2 flux and to compare it with the CO_2 flux calculated with the monthly wind speeds of ERA5.

As fCO_{2atm} is not measured at the mooring, we use the monthly molar fraction of the Ragged Point Barbados (RPB) station located at 13.17°N, 59.43°W where the molar fraction of CO_2, xCO_2, is recorded since November 1987 (http://www.esrl.noaa.gov/gmd/dv/data). The calculation uses the atmospheric pressure and the sea surface temperature measured at the mooring. Atmospheric fCO_2 was measured underway during PIRATA cruises in 2009, 2010 and 2011. The comparison between the atmospheric values at 8°N, 38°W and the RPB values calculated with the atmospheric pressure and the SST measured

during the cruises gives a root mean squared error of 1.0 µatm, which is within the uncertainty of the measurements.

2.3. Model and satellite measurements

The Mercator-Ocean simulation is based on the NEMO modelling platform (Nucleus for European Modelling of the Ocean) and covers the global ocean with a spatial resolution of 0.25° over the 1993–2019 period. The biogeochemical component PISCES (Aumont et al., 2015) is coupled offline to the hydrodynamic NEMO component at a daily frequency. Both components are forced by ERA-Interim atmospheric fields. The biogeochemical simulation is available on the Copernicus marine service catalogue (product GLOBAL_REANALYSIS_BIO_001_029). The detailed features of this simulation are described in the Quality Information Document (http://marine.copernicus.eu/documents/QUID/CMEMS-GLO-QUID-001-029.pdf). The hydrodynamic forcing simulation is available on request at the Mercator-Ocean service desk. We use the daily means of salinity, temperature, inorganic carbon, alkalinity, nutrients, chlorophyll and current fields for the period 2006–2017 for the region 0°–12°N, 55°W–35°W to examine the spatial environment around the mooring.

8-day composites of chlorophyll *a* concentrations from MODIS Aqua at 4 km resolution are used to determine the biological activity close to the mooring site.

Monthly precipitation rate from January to December 2013 is available from the Tropical Rainfall Measuring Mission (TRMM) on a 0.25° × 0.25° grid. The maximum precipitation is a good indicator of the position of the ITCZ.

The surface ocean circulation in 2013 is examined using the OSCAR currents (Bonjean and Lagerloef, 2002) available at https://www.esr.org/research/oscar/oscar-surface-currents/. The OSCAR product is on a 1/3 degree grid on a 5-day time base.

2.4. Lagrangian particle tracking

The surface daily velocity fields of the ocean model run are used together with the Lagrangian particle tracking software ARIANE (Blanke and Raynaud, 1997) to examine the origin of waters reaching the station 8°N-38°W during the period 2 September–5 November corresponding to the decrease in SSS.

Virtual Lagrangian particles are seeded within the site neighbouring cells (within a 1.75° distance) of the model grid (at the surface only), at a resolution of 1/12° – i.e. at higher resolution than the model grid with 9 particles per grid cell, and advected backwards in time for a duration of 90 days. Particles are released every 3 days across the period, constituting a series of 22 releases of 1383 particles amounting to a total of 30,426 particles released for the period. The resolution of particle releases in space and time, together with the extent around the mooring site, enable to obtain a comprehensive cloud of potential water trajectories reaching the site. This experiment is repeated every year for the period 2006–2017. For each trajectory, four variables are recorded at every position; temperature, salinity, inorganic carbon and chlorophyll.

3. Results

3.1. Hydrological setting in 2013

The mooring at 8°N, 38°W is located in the North Equatorial Counter Current (NECC), a surface zonal current that flows eastwards between 3°N and 10°N (Fonseca et al., 2004). The NECC is formed by the North Brazil Current (NBC) and the North Equatorial Current (NEC). It is well developed in summer and reaches its maximum velocity (Richardson and Reverdin, 1987) while it is weaker during the first period of the year and is even replaced by a westward flow in spring (Garzoli and Katz, 1983). The maps of March and September 2013 illustrate the seasonal variations of the surface current field using the OSCAR product, and of the distribution of SSS using the SMOS data (Fig. 2).

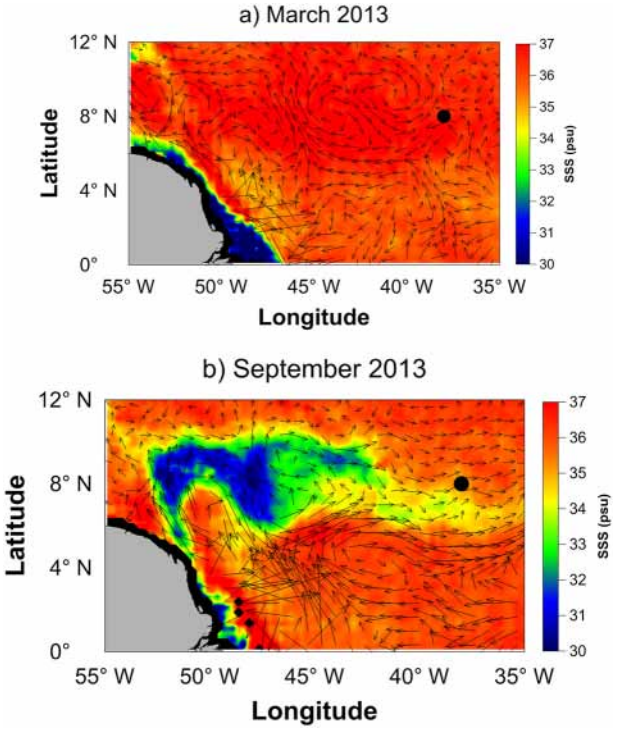

Fig. 2. Surface ocean circulation showing the spread of low salinity water during autumn. Surface currents from OSCAR are superimposed on the SMOS salinity fields for a) March 2013 and b) September 2013. The position of the mooring is indicated by the black dot.

Averaging the zonal velocity in the 5°N–8°N, 45°W–35°W region gives a good estimate of the strength of the NBC retroflection (Grodsky et al., 2014). Following this criteria, we calculate the zonal velocity for the year 2013. From January to June 2013, the zonal velocity is weak and even negative (westward) ranging from −0.16 m/s to 0.15 m/s with a mean of −0.045 ± 0.097 m/s. Very low salinities (< 31 psu) are observed close to the coast of South America and originates at the equator near the Amazon mouth. In March 2013, a water mass of low salinities (< 35 psu) flows northwards along the coast, towards the Caribbean (Fig. 2a). At the mooring, the SMOS SSS is about 36 psu. The meanders and rings of the NBC are visible on the maps. For example, near the coast around 8°N–10°N, in March 2013, a core of high salinity is surrounded by low salinity water (Fig. 2a).

From July to December 2013, when the NECC is well developed, the zonal velocity is always positive (i.e. eastward) ranging from 0.14 m/s to 0.37 m/s with a mean of 0.247 ± 0.075 m/s. The maximum zonal velocity is reached in September 2013, which is consistent with previous studies (e.g. Garzoli et al., 2004). In September 2013, the retroflection of the NBC is well visible by low salinity waters transported to the mooring (Fig. 2b). Between 8°N and 10°N, the NBC becomes detached from the coast and turns eastward, transporting a water mass of salinity 30–31 psu. South of this water mass, values of high salinity close to 36 psu are observed and are typical of surface tropical oceanic water. Within the NECC, the salinity increases gradually towards the east as the low salinity water mass mixes with tropical oceanic water during its journey. As shown by the March and September maps (Fig. 2), the seasonal variations of the surface currents affect the distribution of the SSS in the Western tropical Atlantic, and in particular the mooring site.

In addition to the surface ocean circulation, the SSS at the mooring is also affected by the seasonal migration of the ITCZ. The position of the ITCZ can be detected as the region of maximum precipitation. Each

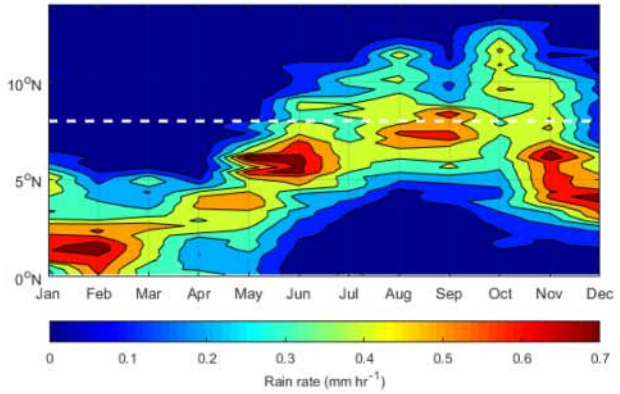

Fig. 3. Maximum precipitation indicating the migration of the ITCZ. TRMM precipitation (in mm h^{-1}) is plotted from 0°N to 15°N along 38°W in 2013. The white dashed line corresponds to the location of the mooring at 8°N.

year, the ITCZ migrates from boreal Spring when it is located at its southernmost position, close to the equator, to its northernmost position, about 10°N, reached in July (Gu and Adler, 2006). According to Tzortzi et al. (2013), the western tropical Atlantic displays a strong seasonal SSS signal, with the maximum SSS in February and the minimum in August, that varies in phase with precipitation.

In 2013, at 8°N, 38°W, the ITCZ is present during the months of August to September as shown by the highest precipitation from TRMM (Fig. 3). Nevertheless, precipitation occurs on a wider period, from May to November due to the width of the ITCZ. From December to April, there is no precipitation at 8°N as the ITCZ is further south, close to the equator.

The comparison of the daily TRMM precipitation of 2013 indicates that the month of September is not significantly different from any other month of the rainy season, using a Wilcoxon rank-sum test. The hypothesis that the median are equals cannot be rejected at the 5% level (p-values ranging from 0.08 to 0.43 for June to November 2013). The months from June to November 2013 define the rainy season and are significantly different from the months from December to May, which corresponds to the dry season at 8°N, 38°W.

3.2. Variability at the mooring in 2013

The CO_2 sensor at 8°N, 38°W transmitted hourly data from the 19th of June until the 13th of October 2013 (Fig. 4a). Variations of fCO_2 are affected by variations of temperature and salinity. A decrease of salinity due to precipitation would cause a decrease of carbon properties by dilution. Warming of surface waters increases fCO_2 by 4%/°C, everything else being constant (e.g. Takahashi et al., 1993). From June to September 2013, the fCO_2 varies slightly around a mean value of about 400 µatm (Fig. 4a). During that period, the daily means of fCO_2, SSS and SST are respectively 396.3 ± 8.9 µatm, 35.43 ± 0.31 psu, and 28.23 ± 0.29 °C. In September 2013, fCO_2 decreases sharply by about 50 µatm and subsequently increases to reach a mean value of 400.5 ± 4.8 µatm in October. The decrease of fCO_2 corresponds to a decrease of SSS by over 2 psu. The SSS minimum of 33.2 psu is reached on 24 September 2013 (Fig. 4b) and coincides with the lowest daily fCO_2 of 361 µatm. Then, the SSS increases gradually to reach 36 psu in December. The SST exhibits small variability around 28.2 °C until September (Fig. 4c) then, from September to December, SST and SSS vary in opposite direction with a correlation coefficient of −0.81. The lowest salinities (< 34 psu) are associated with the highest SST (> 29 °C). They occur in September and are concomitant with the lowest fCO_2. SSS and SST have opposite effects on fCO_2 but the dominant process is salinity, which explains the decrease of fCO_2. After reaching its minimum value, the fCO_2 increases faster than the salinity that remains below 35 psu in October.

Over the whole period of observations, fCO_2 varied by 63 µatm (June–October), SSS by 2.87 psu and SST by 3.37 °C (June–December).

High frequency variability is visible on hourly data of fCO_2, SSS and SST (Fig. 4a, b, c, in red) as previously observed and studied by Bruto et al. (2017). Low salinity peaks correspond to rainfall events and the dilution causes a decrease of surface fCO_2. Near the end of June 2013, a particularly strong decrease of hourly fCO_2 and hourly SSS is observed on a short period of time, which leads to low fCO_2 (< 350 µatm) and salinity (34 psu).

Peaks of hourly SST are mostly observed when the temperature is higher than 28 °C under conditions of clear sky, low wind and strong ocean stratification.

As no biological parameter is measured at 8°N, 38°W, we use the chlorophyll *a* concentration from MODIS. In 2013, the chlorophyll *a* at the mooring is quite low with concentrations always below 0.28 mg m^{-3} (Fig. 5). The lowest concentrations are observed from January to August. In September, the chlorophyll *a* increases abruptly to reach a maximum of 0.26 mg m^{-3} followed by a sharp decrease to remain at concentrations between 0.13 and 0.18 mg m^{-3}. From October to December, the chlorophyll concentrations, although quite low, are significantly higher than the concentrations from January to August (*t*-test, $p < 0.0001$).

As no wind speed is available at the mooring in 2013, the flux of CO_2 is calculated with available wind speed products. As expected, the daily CCMP wind speeds exhibit much more variability compared to the monthly ERA5 wind speeds (Fig. 6a). The comparison between the daily CCMP wind speeds averaged monthly and the ERA5 monthly wind speeds shows that these two wind products are similar (paired t-test, p-value = 0.075). The daily CO_2 flux calculated with the monthly wind speed is smoother (Fig. 6b) and gives a lower mean value (0.65 ± 0.47 mmol m^{-2} day^{-1} over June–October 2013) compared to the flux calculated with the daily wind speeds (0.75 ± 0.86 mmol m^{-2} day^{-1}). The direction of the flux (source or sink to the atmosphere) depends on the difference between the seawater and the atmospheric fCO_2, and the magnitude of the flux depends on the intensity of the wind. The flux shows similar variations as the seawater fCO_2 with a decrease in September (Fig. 6b). From July to October, the monthly wind is weak with a mean of 4.19 ± 0.46 m/s. Although the daily SSS and fCO_2 are the lowest in September, the lowest flux occurs in June because of the strong wind reaching a speed of 6.81 m/s. As a result, the daily flux has the strongest positive and negative values in June. The negative flux is observed when low SSS and fCO_2 are measured and the wind affects its magnitude.

Overall, using the monthly wind speeds, the mooring site is a source of CO_2 to the atmosphere with a mean value of 0.71 ± 0.49 mmol m^{-2} day^{-1}. The decrease of seawater fCO_2 observed in September leads to some CO_2 absorption. It remains small as the wind reaches its lowest speed of 3.70 m/s in September. During the months of January to May and November to December, the wind is significantly stronger than from July to October with a mean of 8.12 ± 0.98 m/s (*t*-test, $p < 0.0001$).

3.3. Model simulations

The model results at 8°N, 38°W in 2013 show a decrease of SSS in September corresponding to the decrease of observed SSS and fCO_2 (Fig. 7). The model underestimates the SSS by about 0.5 psu. The modelled SSS minimum is below 33 psu and is reached on the 15 September. It is followed by an abrupt increase of SSS whereas the observations show a more gradual increase of SSS. Nevertheless, the main patterns of SSS are similar to the observations. The sharp SSS decrease is concomitant to the fCO_2 decrease.

The mixed-layer of the model is calculated using a density criterion of 0.01 kg m^{-3}. At 8°N, 38°W the model has a shallow mixed layer slightly deeper than 50 m from December to February that decreases to reach about 10 m from June to October. It is in good agreement with

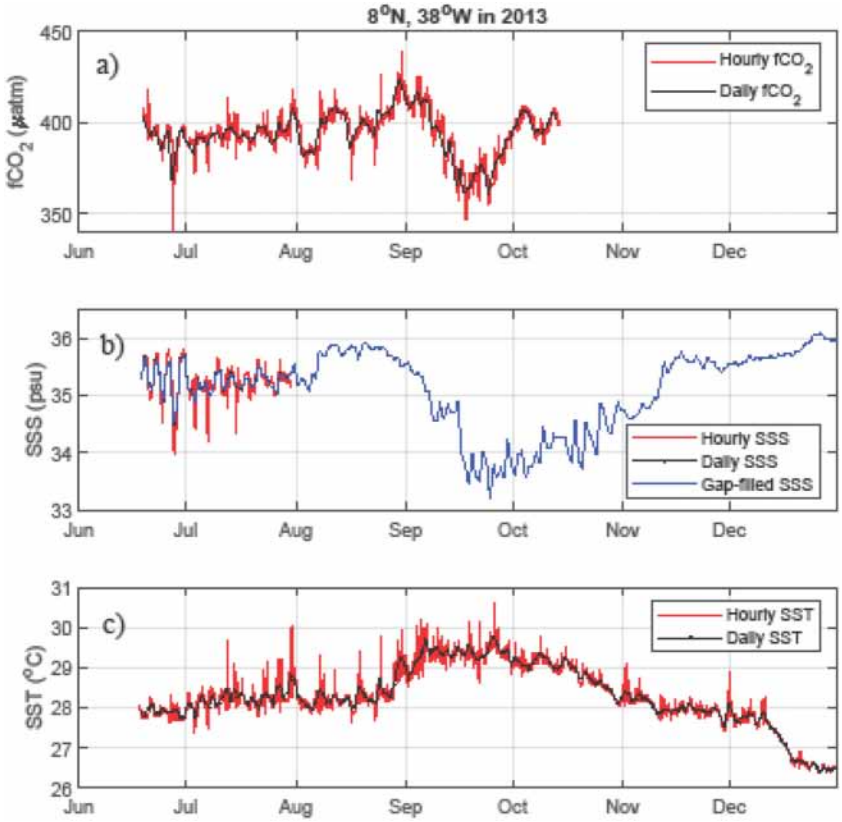

Fig. 4. Variations of hourly (in red) and daily (in black) a) fCO_2, b) SSS and c) SST at 8°N, 38°W in 2013. In b) the blue line corresponds to the daily SSS reconstructed from the salinity at 20 m. (For interpretation of the references to color in this figure legend, the reader is referred to the web version of this article.)

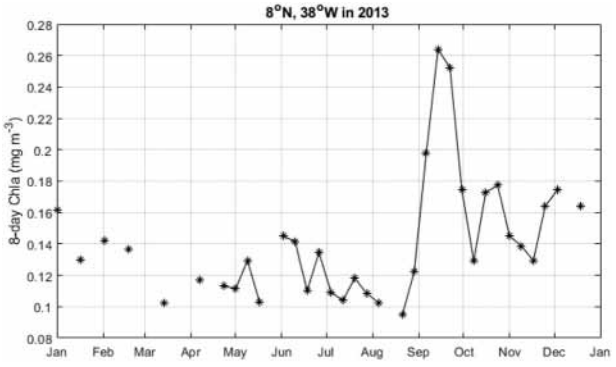

Fig. 5. Seasonal variations of chlorophyll at 8°N, 38°W in 2013 showing the sharp increase of chlorophyll in September. Chlorophyll a ($mg\,m^{-3}$) data are from MODIS.

the mixed layer climatology of de Boyer Montégut et al. (2004) that gives a mixed layer of 14.4 ± 1.5 m from June to October and close or deeper to 50 m during the first period of the year at 8°N, 38°W.

There is no nitrate (NO_3) throughout the year 2013 except in September when a small peak (< 0.1 µmol/kg) appears and is associated with an increase of silicates (SiO_4) from 2 to 5 µmol/kg (Fig. 8a). The silicate concentrations decrease slowly from October whereas the nitrates are rapidly depleted. The distribution of DIC is similar to the distribution of TA with a relatively constant concentration from December to June and lower values from June to November (Fig. 8b). From the beginning of September, both DIC and TA decrease suddenly by over 60 µmol/kg and 80 µmol/kg respectively to reach a minimum on 15 September 2013. The SST exhibits a seasonal cycle with the highest values (> 29 °C) in September and the lowest in February (Fig. 8c). The amplitude of the seasonal cycle is less than 2.57 °C. It is in good agreement with the PIRATA SST data.

3.4. Water origin

The tracking of water parcels shows the influence of the NECC, the NBC and the SEC (in backward order) for the September–November period of the year (Fig. 9a and b, Supplementary material), with particles within the SEC reaching the NBC between 4°S and 2°N.

For 2013, a large number of backtracked particles show low salinity levels nearby the Amazon shelf (Fig. 9c). Typical trajectories of such particles show a sudden drop in both salinity and inorganic carbon when travelling northward in the NBC and passing in front of the Amazon estuary (Fig. 9c). This occurs between 50 and 65 days prior to reaching the station 8°N 38°W, with values slowly rising as particles travel to the station. Note also that a moderate peak in chlorophyll develops soon after the passing in front of the shelf.

Waters from the Amazon show much lower salinity values than waters coming from elsewhere and contribute to setting the low salinity levels at 8°N38°W.

The proportion of particles with low salinity, when passing in front of the Amazon shelf, vary annually, with the largest proportion found for the years 2006, 2008, 2009, 2010 and 2017 (Fig. 9d). The years 2009 and 2014 show high and low proportion of low salinity particles respectively (Fig. 9a, b).

4. Discussion

4.1. Origin of the fCO_2 decrease in September 2013

With the exception of the month of September 2013, the daily fCO_2 at 8°N, 38°W is relatively constant around 400 µatm from June to October, with a mean of 396.8 ± 9.5 µatm. The decrease of fCO_2

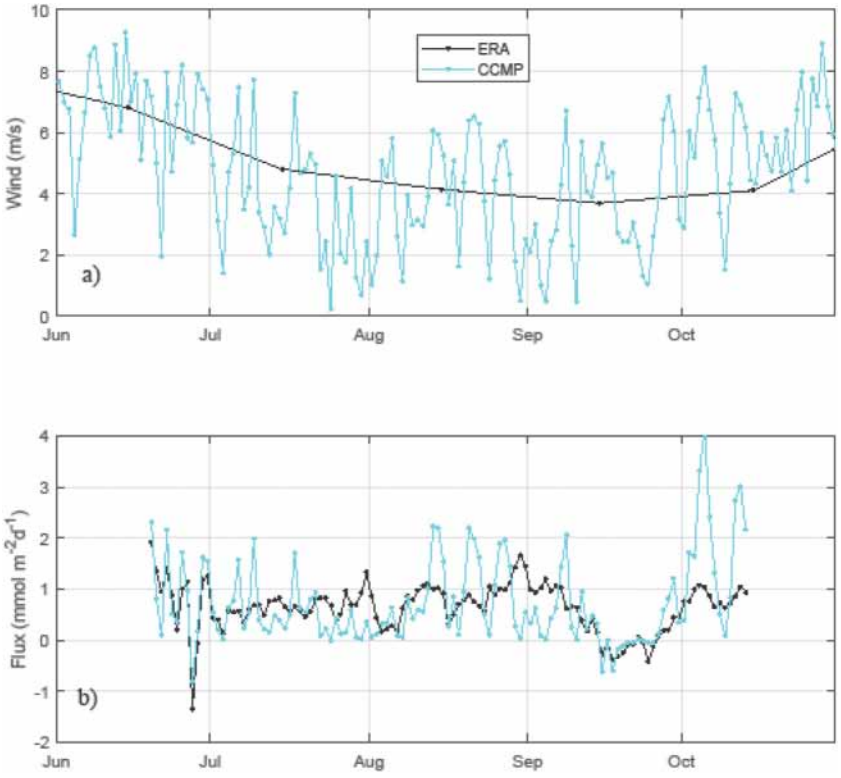

Fig. 6. Decrease of the daily CO_2 flux at 8°N, 38°W in September 2013 at the time of the lowest wind speed. a) Monthly and daily wind speed are from ERA5 (black) and CCMP2 (cyan) products respectively. b) The daily flux of CO_2 is calculated with the monthly ERA5 wind speed (in black) and with the daily CCMP wind speed (cyan). Positive values of the flux correspond to a source of CO_2 to the atmosphere. (For interpretation of the references to color in this figure legend, the reader is referred to the web version of this article.)

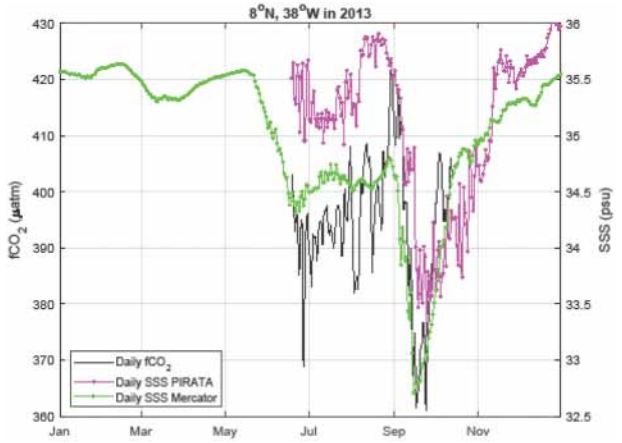

Fig. 7. Modelled SSS, oceanic fCO_2 and SSS observations in 2013 at 8°N, 38°W decreasing at the same time in September.

observed in September is associated with a decrease of salinity. The lowest SSS are associated with the highest SST. Both the ITCZ and the Amazon plume are characterized by low SSS and high SST.

In September 2013, the ITCZ is located at the mooring and the rainfall is strong but similar to the rainfall from June to November. According to the salinity budget of Foltz et al. (2015) at 8°N, 38°W, from June to December, the salinity is affected mainly by rainfall due to the presence of the ITCZ balanced by horizontal advection. They consider that the mooring is at the easternmost location of the spatial extent of the Amazon plume so that the plume only occasionally reaches the mooring. They mention the possible arrival of the Amazon plume for some years, such as 2009 and 2011, but the year 2013 was not mentioned.

Nevertheless, as precipitation levels in September 2013 are not higher compared to the other months of the rainy season, the sudden drop of salinity is likely caused by the Amazon plume, given that, during September, the zonal current is maximum. Previous studies have shown the propagation of the Amazon in the Atlantic. For example, examining satellite images of chlorophyll and CDOM distributions for 1997–2002, Hu et al. (2004) reported that the Amazon water turned eastward at about 9°N during June–August and reached 35°W in late September. Using a 1/6° model, Coles et al. (2013) conclude that the Amazon plume and rainfall have similar impact on the seasonal cycle in the Western Tropical Atlantic and in particular at 8°N, 38°W. The Lagrangian experiment shows that most of the particles released at the mooring site in September–October come from the Amazon shelf unlike other months of the year (see the Supplementary material for the seasonal variability of the origin of the particles, Fig. S2). The salinity drops when particles transported by the SEC arrive at the Amazon shelf (Fig. 9c). Then, their salinities increase slowly until they reach the station 8°N, 38°W in September 2013.

The propagation of the Amazon plume affects not only the distribution of SSS but also the nutrient load and therefore the chlorophyll *a* concentration. In 2013, the maximum daily discharge at Obidos, a station about 600 km of the Amazon mouth (Callede et al., 2004), occurs in early July. At this time, the NBC starts its retroflection and the Amazon plume is transported eastward. The minimum SSS at 8°N, 38°W is observed mid-September. This corresponds to a travel time of about 2 months for the Amazon plume to arrive at the mooring. This is consistent with the work of Coles et al. (2013) who calculated a time of about 40–60 days to reach 40°W-35°W for drifters advected away from the river mouth, using the 1/6° HYCOM model.

The mixing of the Amazon River with oceanic water leads to strong biological activity and the productive waters are advected by the surface currents. They can be detected from satellite by their chlorophyll concentration. The chlorophyll is very high close to the river mouth and the coast ($> 0.8\,mg\,m^{-3}$), then it gradually decreases during the transport of the water (Fig. 9). In September 2013, the mooring is slightly affected by the plume and the chlorophyll concentration at the site is around 0.2–0.3 $mg\,m^{-3}$ (Figs. 5 and 10). Further east, in the NECC, the chlorophyll concentrations are close to zero and there is no sign of biological activity.

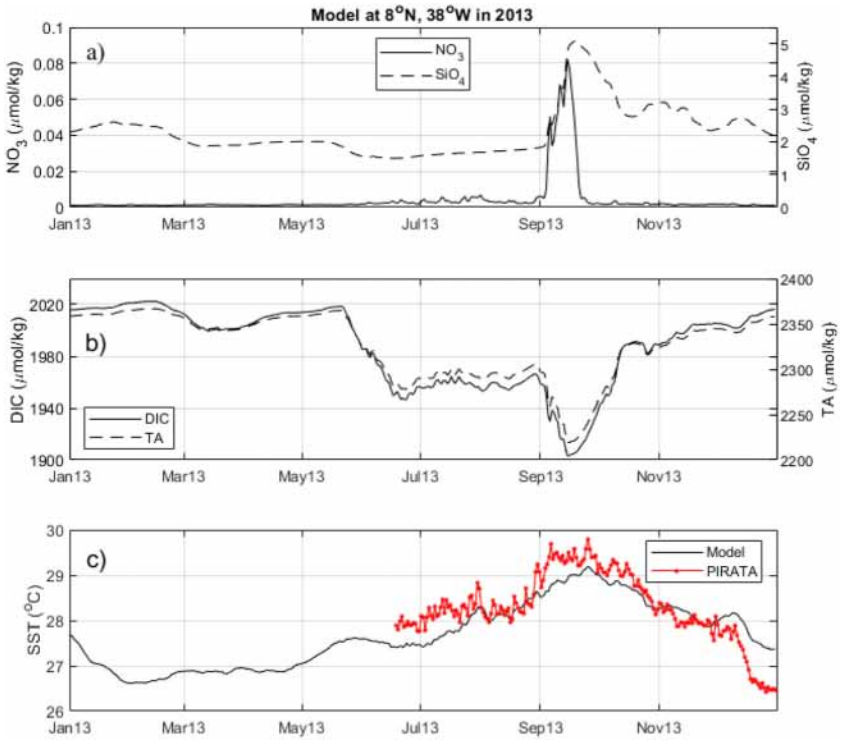

Fig. 8. Model simulations of a) NO_3, SiO_4, b) DIC, TA and c) SST at 8°N, 38°W in 2013 showing the biological signal in September. The SST observations at PIRATA (in red) are included for comparison with the modelled SST. (For interpretation of the references to color in this figure legend, the reader is referred to the web version of this article.)

Although the model does not reproduce the magnitude of the chlorophyll concentration and of the salinity, it captures well the timing of the salinity decrease and chlorophyll increase. At the same time, nitrates and silicates increase to reach their maximum concentration on 15 September 2013, while the carbon parameters (DIC, TA) decrease to their minimum concentrations. The calculation of fCO_2 from modelled DIC and TA gives a higher value than the observed fCO_2. Using DIC and TA to calculate fCO_2 gives the largest error on fCO_2 as DIC and TA covary (McLaughlin et al., 2015). Previous studies show that including pH as an input parameter gives a better estimate of fCO_2 (e.g. Hoppe et al., 2012; Millero, 1995). The correlation coefficient between DIC and TA is higher than 0.97 for the samples and higher than 0.99 for the model. The model usually underestimates DIC and TA by 15 µmol/kg for the lowest discrepancy. The propagation of these errors to calculated fCO_2, using the routine of Orr et al. (2018), gives an error of about 35 µatm. Moreover, underestimating DIC would underestimate fCO_2 but underestimating TA would counteract this effect because a decrease of alkalinity increases fCO_2. The fCO_2 calculated from modelled DIC and TA is then much smoother than the observed fCO_2. In addition, as the modelled chlorophyll concentration is much lower than the satellite chlorophyll, this suggests that the model underestimates the biological productivity, which leads to a lower carbon consumption. The model fails to reproduce the magnitude of the chlorophyll in September 2013. This can either be due to the Amazon plume that is not rich enough in limiting nutrients (the model uses climatological river inputs) or to the assumption of fixed elemental ratios in the biogeochemical model (Redfield ratios for phytoplankton). A variable stoichiometry model (Quota model) could be used to explore this hypothesis. Such models lead to higher biological production than model using a fixed Redfield ratio (e.g. Christian, 2005; Flynn, 2010). Nevertheless, the biological signature is present in the model and in the observations, which gives additional evidence that the Amazon plume arrives at the mooring in September 2013.

4.2. Impact on the variability of the CO_2 flux at seasonal and interannual timescales

The monthly CO_2 flux at 8°N, 38°W reaches its lowest value in September 2013 with a mean of 0.34 ± 0.49 mmol m^{-2} day^{-1}. The flux is at its lowest value compared to the other months because of the decrease of fCO_2 associated with the low salinity water mass. According to Foltz et al. (2015), the Amazon plume arrives at the mooring in 2011. The fCO_2 series of 2011 covers the period from 3 September to 31 December (Bruto et al., 2017) and, in September 2011, the CO_2 flux is similar to the September 2013 value with a mean of 0.34 ± 0.28 mmol m^{-2} day^{-1}. Although there is no long CO_2 record at this mooring, the few data available show high fCO_2 values leading to CO_2 outgassing. According to Bruto et al. (2017), the SST variations drive the fCO_2 variability during the first period of the year. Although there is evidence of the strong correlation between fCO_2 and salinity for the second half of the year, when the ITCZ is present and when the NECC is well developed, an fCO_2-SSS relationship valid for a long period could not be determined.

The salinity minimum observed in September 2013 at the mooring occurs every year at the same time when the NECC transports the Amazon plume and when the ITCZ is present. This minimum shows a significant variation from year to year as previously reported by Foltz et al. (2015). As an example, the PIRATA and MERCATOR series from 2006 to 2017 are presented (Fig. 11a). The minimum of SSS observed at 8°N, 38°W varies between 31 in 2009 to 33.5 in 2014.

The WTA is known to exhibit interannual variability. Indeed, some of the Pacific ENSO events affect the distributions of SST, SSS and biogeochemical properties of the tropical Atlantic (e.g. Lefèvre et al., 2013; Wang, 2005). According to the amount of rainfall, the Amazon basin is subject to droughts and floods (Marengo et al., 2011; Marengo et al., 2012) that affect the freshwater supply to the Atlantic. Among these events, the year 2009 is characterized by an exceptional Amazon flood, tied to a La Niña event in the Pacific, that led to an intense discharge into the WTA (Chen et al., 2010; Tyaquiçã et al., 2017). Although the SSS in 2009 is the lowest of the time-series at 8°N, 38°W, the interannual variations of the Amazon discharge cannot fully explain the

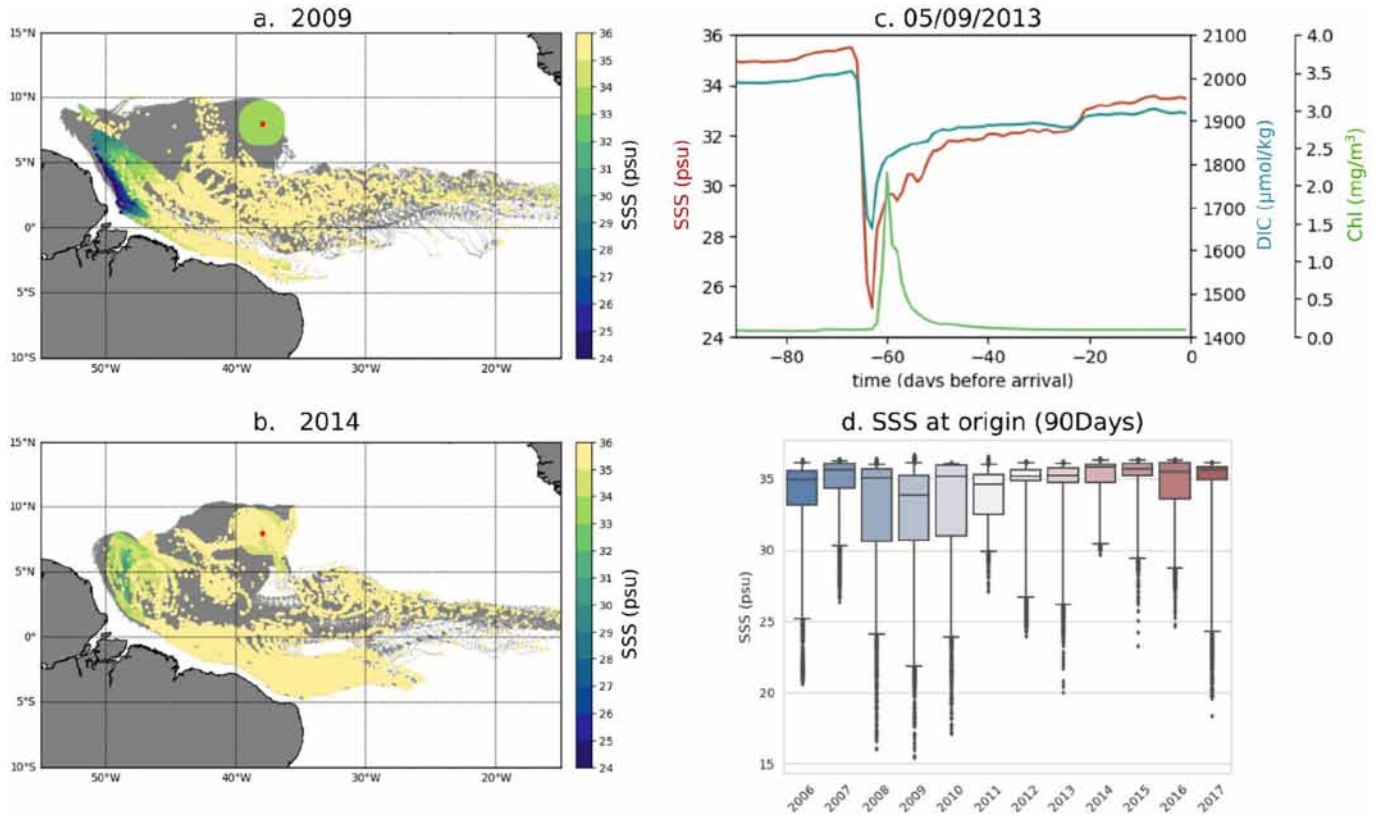

Fig. 9. Example of surface pathways of ocean model particles released uniformly within 1.75° from the station 8°N, 38°W during the period 2nd September–5th November for the years 2009 (a) and 2014 (b), years for which minimum and maximum salinity are recorded, respectively. Particles are backtracked in time for 90 days with trajectories represented in grey and particles position of origin colored according to the salinity value. Note the low salinity values for particles downstream of the Amazon shelf. Particle's release positions around 8°N, 38°W in red (colored circle) are colored according to the mean salinity level for the release period. (c) Example of SSS, DIC and chlorophyll values along a particle trajectory flowing northward in the NBC, crossing the Amazon shelf, and reaching 8°N, 38°W on the 5th of September 2013 through the NECC. (d) Box plot of the interannual variability of salinity levels for particles at origin (90 days prior to reach 8°N, 38°W). Whiskers correspond to the 1st and 99th percentiles. Note the influence of low salinity levels corresponding to the Amazon plume for the years 2008, 2009 and 2010 where minima in salinity are observed at 8°N, 38°W. (For interpretation of the references to color in this figure legend, the reader is referred to the web version of this article.)

minimum SSS variations.

The model is forced by constant seasonal river discharge and reproduces well the variability of this salinity minimum even though the magnitude of the SSS decrease may be slightly different. The other factors that may affect the SSS are the local rainfall, due to the presence of the ITCZ, and the surface ocean circulation. However, we could not find a direct relationship between local rainfall and the salinity minimum. In fact, in 2009 the mean annual rainfall at 8°N, 38°W is the lowest of the 2006–2017 series. A wavelet analysis of the rainfall at 8°N, 38°W did not show stronger variance of the signal in 2013 over the 2006–2017 period. Most of the SSS variability at this site is likely caused by ocean circulation. Urbano et al. (2008) describe the surface circulation of the region as very complex with a two-core structure for the NECC. In addition, this current displays interannual variations (e.g. Fonseca et al., 2004; Hormann et al., 2012). Hormann et al. (2012) also identify north-south shifts of the NECC in response to the meridional and zonal climate modes of the tropical Atlantic. The Lagrangian experiment shows that the salinity decrease observed each year at 8°N, 38°W is explained by the salinity of the water mass originated from the SEC, 90 days before (Fig. 9d), and transported by the NBC and the NECC, as the same salinity pattern is observed (Fig. S3). The salinity varies from year to year with the lowest salinity occurring in 2009 and

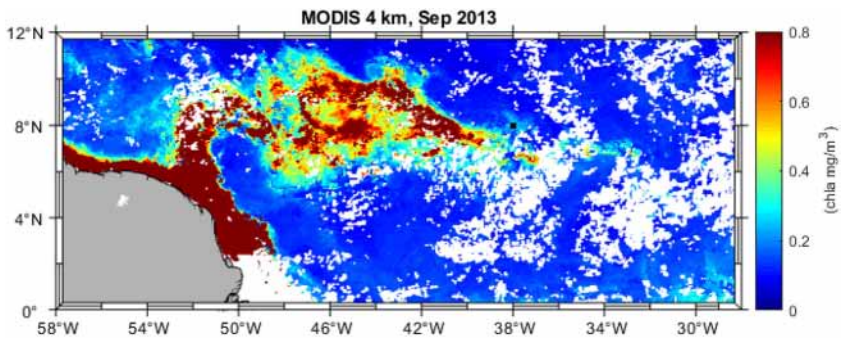

Fig. 10. Advection of high chlorophyll *a* waters, within the NECC, in September 2013, reaching the mooring at 8°N, 38°W (represented by a black square).

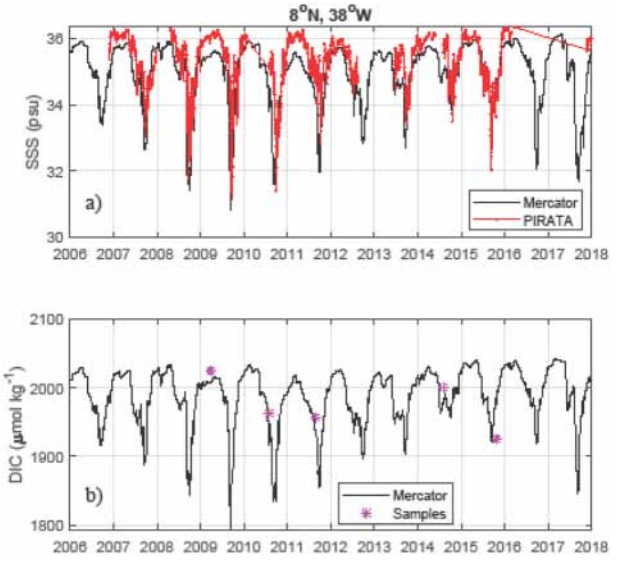

Fig. 11. Interannual variability of observations reproduced by model simulations. Evolution of daily a) SSS and b) DIC at 8°N, 38°W from the model (in black). The model is compared to a) the surface salinity sensor at the mooring (red) and b) to the samples taken for DIC analyses during the PIRATA cruises (magenta). (For interpretation of the references to color in this figure legend, the reader is referred to the web version of this article.)

the highest in 2014. We can see on Fig. 9d that in 2009 there are many more very low SSS values (outliers) than in 2014. These outliers influence the mean salinity at 8°N, 38°W 90 days later.

Although the salinity minimum in September 2013 was not as low as in 2009 or 2011, the fCO_2 variations show that the Amazon plume also arrives at the mooring in 2013, which is confirmed by the Lagrangian experiment. Using satellite data and empirical surface salinity model over the period 2002–2017, Gouveia et al. (2019) conclude that the export of the Amazon plume water has intensified in recent years. Their study area is bounded at 40°W and the Amazon plume reaches 40°W each year from 2009 to 2017. In fact, as reported by Cooley et al. (2007), the carbon deficit induced by the biological activity can persist even though the physical structure of the plume is no longer detectable. Even if the presence of the Amazon plume is difficult to detect because the salinity is close to open ocean values, it takes time to equilibrate the surface water with atmospheric CO_2 (Jones et al., 2014). After strong CO_2 drawdowns associated to the biological activity within the river plume, the CO_2 content of the water mass will gradually increase to reach CO_2 equilibrium with the atmosphere. This process is of the order of the month (Broecker and Peng, 1974).

From the fCO_2 observations only, it is difficult to conclude that the fCO_2 decrease will take place each year at the mooring because of the short record. As the model reproduces the salinity variations and some impact of the Amazon propagation in September 2013, we examine the simulations of DIC from 2006 to 2017 (Fig. 11b). The modelled SSS is strongly correlated to DIC ($r = 0.96$). The DIC minimum coincides with the SSS minimum. In addition, the lowest DIC value occurring in 2009 corresponds to the lowest SSS observed in 2009. Although very few DIC data are available at this site, the samples collected are in reasonable agreement with the modelled DIC values. The CO_2 properties are influenced by the SSS variability in autumn, which suggests that the fCO_2 decrease is likely to be observed each year around September–October.

This high natural variability of the tropical Atlantic makes it difficult to determine the evolution of the source of CO_2 to the atmosphere. A network of instrumented moorings covers the tropical Atlantic and monitors the meteorological (wind, rainfall, air temperature, atmospheric pressure, radiation) and oceanic (temperature, salinity) properties but monitoring of biogeochemical properties is rare (Foltz et al., 2019). The biogeochemical properties of the tropical Atlantic are still undersampled and more measurements are required to improve the estimates of the CO_2 flux for the global carbon budget. At first order, decreasing SSS in the tropics would probably lead to a decrease of the CO_2 source because of the relationship between these two parameters. However, SSS changes might affect other parameters. For example, Jahfer et al. (2017) report that a considerable reduction in Amazon runoff would result in cooling the equatorial Atlantic. The cooling would decrease fCO_2 and tend to counteract the fCO_2 increase associated with a salinity increase. Nevertheless, the CO_2 budget is likely to be affected by SSS and SST changes in the tropics and the evolution of the tropical source of CO_2 remains difficult to predict.

5. Conclusions

From June to October 2013, the hourly fCO_2 measured at 8°N, 38°W is relatively constant except in September 2013 when fCO_2 decreases rapidly by 50 µatm. The lowest fCO_2 of 361 µatm, reached on 24 September 2013, corresponds to the lowest salinity of 33.2 psu. In fall, two main processes decrease the SSS at the mooring. First, high precipitation caused by the presence of the ITCZ leads to SSS values lower than 35 psu. Secondly, the retroflection of the NBC starting in July feeds the NECC with Amazon waters. In September 2013, the NECC is well developed and strong so that the Amazon plume can reach 8°N, 38°W. This explains a further decrease of SSS but the main feature is the biological imprint in the water mass. MODIS data exhibit a peak of chlorophyll over 0.2 mg m^{-3} at 8°N, 38°W in September 2013. The advection of the Amazon plume is visible from the MODIS image in September with the highest chlorophyll concentrations near the Amazon mouth that decrease eastward during the water transport within the NECC. The Lagrangian experiment confirms that most of the particles released at the mooring site in September–November come from a water mass passing close to the Amazon shelf. Although the model does not reproduce the magnitude of the chlorophyll, the distribution over time is similar with a peak in September. In addition, modelled nutrients exhibit peak values while DIC and TA are at their lowest concentrations at the same time. The simulations over the 2006–2017 period highlight the interannual variability of the SSS minimum, as previously reported, but also the strong correlation between DIC and SSS ($r = 0.96$). Overall, the site is a source of CO_2 to the atmosphere of 0.65 ± 0.47 mmol m^{-2} day^{-1} from June to October 2013. Ignoring September, the mean CO_2 flux is 0.76 ± 0.41 mmol m^{-2} day^{-1}. The impact of the fCO_2 decrease in September remains moderate because the wind is at its lowest intensity during this month. As SSS is an important driver of the carbon parameters, future variations of the water cycle, by changes in river discharge and/or rainfall, are likely to affect the CO_2 budget in the tropical Atlantic.

Declaration of competing interest

The authors declare that they have no known competing financial interests or personal relationships that could have appeared to influence the work reported in this paper.

Acknowledgments

The CO_2 observations have been funded and maintained by the European Integrated Projects CARBOOCEAN (contract 511176-2), CARBOCHANGE (grant agreement 264879), ATLANTOS and the Institut de Recherche pour le Développement (IRD). The data are available in the SOCAT database. We are very grateful to US IMAGO of IRD, and especially to Jacques Grelet and Fabrice Roubaud for their technical support at sea and the deployment of the CARIOCA CO_2 sensor, and to Laurence Beaumont from the DT INSU for preparation

and calibration of the sensor. The SNAPO-CO2 at LOCEAN in Paris analyzed the seawater samples, taken during the Brazilian cruises, for DIC and TA. Data management for PIRATA moorings is conducted by the TAO project office at NOAA/PMEL in collaboration with many research institutes listed on the PIRATA website (www.pmelnoaa.gov/pirata). Precipitation data from the GPCP were downloaded from the Giovanni online data system, developed and maintained by the NASA Goddard Earth Sciences (GES) Data and Information Services Center (DISC). We acknowledge the TRMM mission scientists and associated NASA personnel for production of these data, the OSCAR Project Office for providing the ocean surface current analyses. CCMP Version 2.0 analyses are produced by Remote Sensing Systems and sponsored by NASA Earth Science funding. Data are available at www.remss.com. The NCEP Reanalysis Derived data are provided by the NOAA/OAR/ESRL PSD, Boulder, Colorado, USA, from their Web site at https://www.esrl.noaa.gov/psd/. Chlorophyll a concentrations from MODIS Aqua 4 km were downloaded from the Giovanni online data system, developed and maintained by the NASA Goddard Earth Sciences (GES) Data and Information Services Center (DISC). The manuscript benefited from the comments of two anonymous reviewers.

Appendix A. Supplementary data

Supplementary data to this article can be found online at https://doi.org/10.1016/j.jmarsys.2020.103419.

References

Aumont, O., Ethé, C., Tagliabue, A., Bopp, L., Gehlen, M., 2015. PISCES-v2: an ocean biogeochemical model for carbon and ecosystem studies. Geosci. Model Dev. 8, 2465–2513.

Blanke, B., Raynaud, S., 1997. Kinematics of the Pacific equatorial undercurrent: an Eulerian and Lagrangian approach from GCM results. J. Phys. Oceanogr. 27, 1038–1053.

Bonjean, F., Lagerloef, G.S.E., 2002. Diagnostic model and analysis of the surface currents in the tropical Pacific Ocean. J. Phys. Oceanogr. 32, 2938–2954.

Bourlès, B., Araujo, M., McPhaden, M.J., Brandt, P., Foltz, G.R., Lumpkin, R., Giordani, H., Hernandez, F., Lefèvre, N., Nobre, P., Campos, E., Saravanan, R., Trotte-Duhà, J., Dengler, M., Hahn, J., Hummels, R., Lübbecke, J.F., Rouault, M., Cotrim, L., Sutton, A., Jochum, M., Perez, R.C., 2019. PIRATA: a sustained observing system for tropical Atlantic climate research and forecasting. Earth Space Sci. 6, 577–616.

Broecker, W.S., Peng, T.-H., 1974. Gas exchange rates between air and sea. Tellus 26, 21–35.

Bruto, L., Araujo, M., Noriega, C., Veleda, D., Lefèvre, N., 2017. Variability of CO_2 fugacity at the western edge of the tropical Atlantic Ocean from the 8°N, 38°W PIRATA buoy. Dyn. Atmos. Oceans 78, 1–13.

Callede, J., Guyot, J.-L., Ronchail, J., L'Hote, Y., Niel, H., De Oliveira, E., 2004. Evolution of the River Amazon's discharge at Óbidos from 1903 to 1999. Hydrol. Sci. J. 49, 85–97.

Chen, J.L., Wilson, C.R., Tapley, B.D., 2010. The 2009 exceptional Amazon flood and interannual terrestrial water storage change observed by GRACE. Water Resour. Res. 46.

Christian, J.R., 2005. Biogeochemical cycling in the oligotrophic ocean: Redfield and non-Redfield models. Limnol. Oceanogr. 50, 646–657.

Coles, V.J., Brooks, M.T., Hopkins, J., Stukel, M.R., Yager, P.L., Hood, R.R., 2013. The pathways and properties of the Amazon River Plume in the tropical North Atlantic Ocean. J. Geophys. Res. 118, 6894–6913.

Cooley, S.R., Yager, P.L., 2006. Physical and biological contributions to the western tropical North Atlantic Ocean carbon sink formed by the Amazon River plume. J. Geophys. Res. 111. https://doi.org/10.1029/2005JC002954.

Cooley, S.R., Coles, V.J., Subramaniam, A., Yager, P.L., 2007. Seasonal variations in the Amazon plume-related atmospheric carbon sink. Glob. Biogeochem. Cycles 21. https://doi.org/10.1029/2006GB002831.

de Boyer Montégut, C., Madec, G., Fischer, A.S., Lazar, A., Iudicone, D., 2004. Mixed layer depth over the global ocean: An examination of profile data and a profile-based climatology. J. Geophys. Res. Oceans 109. https://doi.org/10.1029/2004jc002378.

DeMaster, D.J., Pope, R., 1996. Nutrient dynamics in Amazon shelf waters: result from AMASSEDS. Cont. Shelf Res. 16, 263–289.

Edmond, J.M., 1970. High precision determination of titration alkalinity and total carbon dioxide content of seawater by potentiometric titration. Deep-Sea Res. 17, 737–750.

Flynn, K.J., 2010. Ecological modelling in a sea of variable stoichiometry: dysfunctionality and the legacy of Redfield and Monod. Prog. Oceanogr. 84, 52–65.

Foltz, G.R., Grodsky, S.A., Carton, J.A., McPhaden, M.J., 2004. Seasonal salt budget of the northwestern tropical Atlantic Ocean along 38°W. J. Geophys. Res. Oceans 109.

Foltz, G.R., Schmid, C., Lumpkin, R., 2015. Transport of surface freshwater from the equatorial to the subtropical North Atlantic Ocean. J. Phys. Oceanogr. 45, 1086–1102.

Foltz, G.R., Brandt, P., Richter, I., Rodríguez-Fonseca, B., Hernandez, F., Dengler, M., Rodrigues, R.R., Schmidt, J.O., Yu, L., Lefevre, N., Da Cunha, L.C., McPhaden, M.J., Araujo, M., Karstensen, J., Hahn, J., Martín-Rey, M., Patricola, C.M., Poli, P., Zuidema, P., Hummels, R., Perez, R.C., Hatje, V., Lübbecke, J.F., Polo, I., Lumpkin, R., Bourlès, B., Asuquo, F.E., Lehodey, P., Conchon, A., Chang, P., Dandin, P., Schmid, C., Sutton, A., Giordani, H., Xue, Y., Illig, S., Losada, T., Grodsky, S.A., Gasparin, F., Lee, T., Mohino, E., Nobre, P., Wanninkhof, R., Keenlyside, N., Garcon, V., Sánchez-Gómez, E., Nnamchi, H.C., Drévillon, M., Storto, A., Remy, E., Lazar, A., Speich, S., Goes, M., Dorrington, T., Johns, W.E., Moum, J.N., Robinson, C., Perruche, C., de Souza, R.B., Gaye, A.T., López-Parages, J., Monerie, P.-A., Castellanos, P., Benson, N.U., Hounkonnou, M.N., Duhá, J.T., Laxenaire, R., Reul, N., 2019. The tropical Atlantic observing system. Front. Mar. Sci. 6.

Fonseca, C.A., Goni, G.J., Johns, W.E., Campos, 2004. Investigation of the North Brazil Current retroflection and North Equatorial Countercurrent variability. Geophys. Res. Lett. 31. https://doi.org/10.1029/2004GL020054.

Garzoli, S.L., Katz, E.J., 1983. The forced annual reversal of the Atlantic North Equatorial Countercurrent. J. Phys. Oceanogr. 13, 2082–2090.

Garzoli, S.L., Field, A., Johns, W.E., Yao, Q., 2004. North Brazil Current retroflection and transports. Geophys. Res. Lett. 109. https://doi.org/10.1029/2003JC001775.

Gouveia, N.A., Gherardi, D.F.M., Wagner, F.H., Paes, E.T., Coles, V.J., Aragão, L.E.O.C., 2019. The salinity structure of the Amazon River plume drives spatiotemporal variation of oceanic primary productivity. J. Geophys. Res. Biogeosci. 124, 147–165.

Grodsky, S.A., Carton, J.A., Bryan, F.O., 2014. A curious local surface salinity maximum in the northwestern tropical Atlantic. J. Geophys. Res. Oceans 119, 484–495.

Gu, G., Adler, R.F., 2006. Interannual rainfall variability in the tropical Atlantic region. J. Geophys. Res. 111. https://doi.org/10.1029/2005JD005944.

Hood, E.M., Merlivat, L., 2001. Annual to interannual variations of fCO_2 in the northwestern Mediterranean Sea: results from hourly measurements made by CARIOCA buoys, 1995–1997. J. Mar. Res. 59, 113–131.

Hoppe, C.J.M., Langer, G., Rokitta, S.D., Wolf-Gladrow, D.A., Rost, B., 2012. Implications of observed inconsistencies in carbonate chemistry measurements for ocean acidification studies. Biogeosciences 9, 2401–2405.

Hormann, V., Lumpkin, R., Foltz, G.R., 2012. Interannual North Equatorial Countercurrent variability and its relation to tropical Atlantic climate modes. J. Geophys. Res. Oceans 117.

Hu, C., Montgomery, E.T., Schmitt, R.W., Muller-Karger, F.E., 2004. The dispersal of the Amazon and Orinoco River water in the tropical Atlantic and Caribbean Sea: observation from space and S-PALACE floats. Deep Sea Res. II 51, 1151–1171.

Ibánhez, J.S.P., Araujo, M., Lefèvre, N., 2016. The overlooked tropical oceanic CO_2 sink. Geophys. Res. Lett. 43. https://doi.org/10.1002/2016GL068020.

Jahfer, S., Vinayachandran, P.N., Nanjundiah, R.S., 2017. Long-term impact of Amazon river runoff on northern hemispheric climate. Sci. Rep. 7. https://doi.org/10.1038/s41598-41017-10750-y.

Jones, D.C., Ito, T., Takano, Y., Hsu, W.-C., 2014. Spatial and seasonal variability of the air-sea equilibration timescale of carbon dioxide. Glob. Biogeochem. Cycles 28, 1163–1178.

Körtzinger, A., 2003. A significant sink of CO_2 in the tropical Atlantic Ocean associated with the Amazon River plume. Geophys. Res. Lett. 30 (24), 2287. https://doi.org/10.1029/2003GL018841.

Körtzinger, A., 2010. The outer Amazon plume: an atmospheric CO_2 sink. In: Liu, K.K., Atkinson, L., Quiñones, R., McManus, L.T. (Eds.), Carbon and Nutrient Fluxes in Continental Margins: A Global Synthesis. Springer, New York, pp. 450–453.

Lefèvre, N., Moore, G., Aiken, J., Watson, A., Cooper, D., Ling, R., 1998. Variability of pCO_2 in the tropical Atlantic in 1995. J. Geophys. Res. 103, 5623–5634.

Lefèvre, N., Diverrès, D., Gallois, F., 2010. Origin of CO_2 undersaturation in the western tropical Atlantic. Tellus B 62 (5), 595–607 (doi:510.1111/j.1600-0889.2010.00475.x).

Lefèvre, N., Caniaux, G., Janicot, S., Gueye, A.K., 2013. Increased CO_2 outgassing in February–May 2010 in the tropical Atlantic following the 2009 Pacific El Niño. J. Geophys. Res. 118, 1645–1657.

Marengo, J.A., Tomasella, J., Alves, L.M., Soares, W.R., Rodriguez, D.A., 2011. The drought of 2010 in the context of historical droughts in the Amazon region. Geophys. Res. Lett. 38.

Marengo, J.A., Tomasella, J., Soares, W.R., Alves, L.M., Nobre, C.A., 2012. Extreme climatic events in the Amazon basin. Theor. Appl. Climatol. 107, 73–85.

McLaughlin, K., Weisberg, S.B., Dickson, A.G., Hofmann, G.E., Newton, J.A., Aseltine-Neilson, D., Barton, A., Cudd, S., Feely, R.A., Jefferds, I.W., Jewett, E.B., King, T., Langdon, C.J., McAfee, S., Pleschner-Steele, D., Steele, B., 2015. Core principles of the California Current Acidification Network: linking chemistry, physics, and ecological effects. Oceanography 28, 160–169.

Millero, F.J., 1995. Thermodynamics of the carbon dioxide system in the oceans. Geochim. Cosmochim. Acta 59, 661–677.

Orr, J.C., Epitalon, J.-M., Dickson, A.G., Gattuso, J.-P., 2018. Routine uncertainty propagation for the marine carbon dioxide system. Mar. Chem. 207, 84–107.

Richardson, P.L., Reverdin, G., 1987. Seasonal cycle of velocity in the Atlantic North Equatorial Countercurrent as measured by surface drifters current meters and ship drift. J. Geophys. Res. 92, 3691–3708.

Smith, J.R., Demaster, D.J., 1996. Phytoplankton biomass and productivity in the Amazon River plume: correlation with seasonal river discharge. Cont. Shelf Res. 16, 291–319.

Subramaniam, A., Yager, P.L., Carpenter, E.J., Mahaffey, C., Björkman, K., Cooley, S., Kustka, A.B., Montoya, J.P., Sañudo-Wilhelmy, S.A., Shipe, R., Capone, D.G., 2008. Amazon River enhances diazotrophy and carbon sequestration in the tropical North Atlantic Ocean. Proc. Natl. Acad. Sci. 105, 10460–10465.

Sweeney, C., Gloor, E., Jacobson, A.R., Key, R.M., McKinley, G., Sarmiento, J.L., Wanninkhof, R., 2007. Constraining global air-sea gas exchange for CO_2 with recent

bomb ^{14}C measurements. Glob. Biogeochem. Cycles 21. https://doi.org/10.1029/2006GB002784.
Takahashi, T., Olafsson, J., Goddard, J.G., Chipman, D.W., 1993. Seasonal variation of CO_2 and nutrients in the high-latitude surface oceans: a comparative study. Glob. Biogeochem. Cycles 7, 843–878.
Ternon, J.F., Oudot, C., Dessier, A., Diverrès, D., 2000. A seasonal tropical sink for atmospheric CO_2 in the Atlantic ocean: the role of the Amazon River discharge. Mar. Chem. 68, 183–201.
Turk, D., Zappa, C.J., Meinen, C.S., Christian, J.R., Ho, D.T., dickson, A.G., McGillis, W.R., 2010. Rain impacts on CO_2 exchange in the western equatorial Pacific Ocean. Geophys. Res. Lett. 37. https://doi.org/10.1029/2010GL045520.
Tyaquiçã, P., Veleda, D., Lefèvre, N., Araujo, M., Noriega, C., Caniaux, G., Servain, J., Silva, T., 2017. Amazon plume salinity response to ocean teleconnections. Front. Mar. Sci. https://doi.org/10.3389/fmars.2017.00250.
Tzortzi, E., Josey, S.A., Srokosz, M., Gommenginger, C., 2013. Tropical Atlantic salinity variability: new insights from SMOS. Geophys. Res. Lett. 40, 2143–2147.
Urbano, D.F., De Almeida, R.A.F., Nobre, P., 2008. Equatorial Undercurrent and North Equatorial Countercurrent at 38°W: a new perspective from direct velocity data. J. Geophys. Res. 113. https://doi.org/10.1029/2007JC004215.
Varona, H., Velluci, V., Silva, M., Cintra, M., Araujo, M., 2019. Amazon River plume influence on Western Tropical Atlantic dynamic variability. Dyn. Atmos. Oceans 85, 1–15.
Wang, C., 2005. ENSO, Atlantic climate variability, and the walker and hadley circulation. In: diaz, H.F., Bradley, R.S. (Eds.), The Hadley Circulation: Present, Past and Future. Kluwer Academic Publishers, The Netherlands, pp. 173–202.
Wang, X., Murtugudde, R., Hackert, E., Wang, J., Beauchamp, J., 2015. Seasonal to decadal variations of sea surface pCO2 and sea-air CO2 flux in the equatorial oceans over 1984–2013: a basin-scale comparison of the Pacific and Atlantic Oceans. Glob. Biogeochem. Cycles 29, 597–609.
Weiss, R.F., 1974. CO_2 in water and seawater: the solubility of a non-ideal gas. Mar. Chem. 2, 203–215.
Wentz, F.J.J., Scott, R., Hoffman, M., Leidner, R., Atlas, J.A., 2015. Remote Sensing Systems Cross-Calibrated Multi-Platform (CCMP) 6-hourly Ocean Vector Wind Analysis Product on 0.25 deg Grid, Version 2.0. Remote Sensing Systems, Santa Rosa, CA p. Available online at. www.remss.com/measurements/ccmp.
Williams, R.G., Follows, M.J, 2011. Ocean Dynamics and the Carbon Cycle: Principles and Mechanisms. Cambridge University Press.